

A Physically Based Horizontal Subgrid-Scale Turbulent Mixing Parameterization for the Convective Boundary Layer

BOWEN ZHOU AND KEFENG ZHU

Key Laboratory for Mesoscale Severe Weather, Ministry of Education, and School of Atmospheric Sciences, Nanjing University, Nanjing, China

MING XUE

Key Laboratory for Mesoscale Severe Weather, Ministry of Education, and School of Atmospheric Sciences, Nanjing University, Nanjing, China, and Center for Analysis and Prediction of Storms, and School of Meteorology, University of Oklahoma, Norman, Oklahoma

(Manuscript received 7 December 2016, in final form 5 June 2017)

ABSTRACT

Compared to the representation of vertical turbulent mixing through various planetary boundary layer (PBL) schemes, the treatment of horizontal turbulent mixing in the boundary layer has received much less attention. In mesoscale and convective-scale models, subgrid-scale horizontal turbulent mixing has traditionally been associated with mesoscale circulations or eddies. Its parameterization most often adopts the gradient-diffusion model, where the horizontal mixing coefficients are usually set constant, or through the 2D Smagorinsky formulation, or in some cases based on the 1.5-order turbulence kinetic energy (TKE) closure. For horizontal turbulent mixing associated with boundary layer eddies, the traditional schemes are shown to perform poorly. This work investigates the characteristic turbulence velocity and length scales based on analysis of a well-resolved, wide-domain large-eddy simulation of a convective boundary layer (CBL). To improve the representation of horizontal turbulent mixing by CBL eddies, a class of schemes is proposed with different levels of sophistication. The first two schemes can be used together with first-order PBL schemes, while the third uses TKE to define its characteristic velocity scale and can be used together with TKE-based higher-order PBL schemes. The proposed parameterizations are tested a posteriori in idealized simulations of turbulent dispersion of a passive scalar. Comparisons show improved horizontal dispersion by the proposed schemes and further demonstrate the weakness of the existing schemes.

1. Introduction

In the atmospheric boundary layer (ABL), momentum, heat, water vapor, and other scalars are vigorously mixed via turbulent eddies in both horizontal and vertical directions. The length scale of ABL turbulence is of subgrid-scale to mesoscale and large-scale models. Therefore, the effects of turbulent mixing on the resolved flow must be parameterized, although the parameterizations mostly deal with the effects of mixing in the vertical direction. Research and development on the parameterization of vertical turbulent mixing, or commonly known as the planetary boundary layer (PBL) schemes, have been going on since the early work of Blackadar (1962). In the latest release of the Weather

Research and Forecasting (WRF) Model, version 3.8, 11 different PBL schemes are available for research and application purposes.

Compared to its vertical counterpart, horizontal turbulent mixing has attracted much less attention (Byun and Schere 2006; Ito et al. 2014, hereafter INN14). Research on horizontal mixing has been mostly carried out to serve the air quality engineering community on issues concerning the horizontal dispersion of pollutants (Nazaroff and Alvarez-Cohen 2001) and the agricultural and forest meteorology community on footprint modeling of vegetation–atmosphere exchange (Kormann and Meixner 2001). In both cases, the Gaussian plume model is often used to predict the downwind concentration from passive scalar emissions in an idealized environment. The crosswind diffusion is parameterized through the spatial spread (standard deviation) of the

Corresponding author: Ming Xue, mxue@ou.edu

DOI: 10.1175/JAS-D-16-0324.1

© 2017 American Meteorological Society. For information regarding reuse of this content and general copyright information, consult the [AMS Copyright Policy](http://www.ametsoc.org/PUBSReuseLicenses) (www.ametsoc.org/PUBSReuseLicenses).

Gaussian plume. The dispersion parameter is estimated through empirical power-law formulations based on a set of Pasquill–Gifford dispersion coefficients that takes into account of the bulk stability of the atmosphere (Pasquill 1961; Davidson 1990). Recently, horizontal turbulent mixing of momentum and heat is also receiving attention from the tropical cyclone (TC) community, as it has been recognized as one of the most important factors affecting the intensities of simulated TCs (Bryan and Rotunno 2009; Bryan 2012).

More realistic horizontal turbulent mixing due to convective boundary layer eddies was studied through the classic laboratory tank experiments by Willis and Deardorff (1976, 1978, 1981). These experiments are set up to investigate turbulent diffusion of a passive scalar in a horizontally homogenous flow field. In the experiments, the cross-stream dispersion of neutrally buoyant oil droplets was characterized by the same dispersion parameter as the Gaussian plume model and fitted through power-law relations to the downstream advection time normalized by the characteristic time of free convection in the mixed layer. The cross-stream dispersion was measured as a vertically averaged bulk variable through the depth of the mixed layer. Horizontal diffusion at different elevations was not reported.

Despite its usefulness, the Gaussian plume model is an analytical approach for predicting the ensemble-averaged tracer dispersion in a steady-state flow over simple flat terrain. It is inappropriate for general-purpose numerical weather prediction (NWP) or climate models. Parameterizations of horizontal turbulent mixing are quite limited and suffer from a lack of physical basis. This is partly due to the limited physical understanding of the horizontal turbulent mixing processes and partly because the role of horizontal mixing is often undermined by the wide use of numerical diffusion (either associated with the advection schemes or explicitly included as computational mixing) to suppress numerical instabilities.

Current parameterizations of horizontal turbulent mixing in NWP models are often based on the gradient-diffusion assumption, where the horizontal flux is represented by the product of a horizontal turbulent exchange coefficient K_h and the horizontal gradient of the respective variable. The coefficient K_h is most often parameterized either by taking on a constant value or with the 2D Smagorinsky model (Xue et al. 2000; Skamarock et al. 2008). In the first approach, the constant K_h value is set arbitrarily to provide some background mixing and often takes on a small value or even zero because computational mixing or numerical diffusion has already provided a

sufficient amount of horizontal mixing (Weisman et al. 1997). The second approach uses the 2D Smagorinsky formulation to parameterize K_h by taking account of the horizontal stretching and shearing of the mesoscale flow field (Smagorinsky 1963). The 2D version of the Smagorinsky model was initially proposed for use in a general circulation model (GCM). Smagorinsky (1993) laid out the derivation of his parameterization, which essentially relies on a $k^{-5/3}$ mesoscale (10^2 – 10^5 m) horizontal energy spectrum. The observational evidence of $-5/3$ spectral slope in the mesoscale region is presented most notably in Nastrom and Gage (1985). The dynamics responsible for such spectral behavior is still unclear (Skamarock et al. 2014), although it is likely attributed to stratified turbulence (Lilly 1983). Unlike the 3D Smagorinsky model derived by Lilly (1967) for large-eddy simulation (LES) with inertial subrange grid spacings (less than 100 m), the 2D Smagorinsky model for mesoscale spacings is not well established (INN14). Based on its formulation, the 2D Smagorinsky model represents horizontal mixing due to mesoscale circulations or eddies, which are associated with mesoscale horizontal gradients. Horizontal mixing by boundary layer eddies, such as those demonstrated in the Willis and Deardorff tank experiments, are not accounted for.

In the Advanced Regional Prediction System (ARPS) (Xue et al. 2000), the 3D Smagorinsky–Lilly turbulence scheme is available as an option. When the horizontal grid spacing Δ_h is significantly different from the vertical grid spacing Δ_v , the length scale appearing in the eddy mixing coefficient formulation is recommended to be equal to Δ_h and Δ_v for the respective directions. The physical justification of this approach has not been investigated, however. In ARPS, a more commonly used turbulence scheme is the one based on the 1.5-order TKE, which defines the horizontal and vertical mixing lengths differently except for LESs.

In general, it is difficult to obtain reliable measurements of horizontal turbulent fluxes from field measurements. LES, on the other hand, offers a viable approach to study horizontal turbulent mixing. In LES, the large energetic turbulent eddies are directly resolved, and the effects of the smaller subgrid-scale motions on the resolved flow are modeled (Pope 2000). Recently, INN14 used LES to study horizontal turbulent mixing of a passive scalar in a quasi-steady and horizontally homogeneous free convective boundary layer (CBL). By introducing a passive scalar field with a constant horizontal gradient, they were able to quantify horizontal turbulent mixing due to CBL eddies. They found that horizontal turbulent fluxes of the passive scalar are well represented by a gradient-diffusion

model with a universal eddy-diffusivity profile (INN14, their Fig. 3). Based on the work of INN14, we investigate the characteristic horizontal turbulence length and velocity scales of a CBL using high-resolution and wide-domain LES. By quantifying the characteristics of the CBL eddies, physically based horizontal turbulent mixing parameterizations for CBL eddy-induced horizontal mixing are proposed and tested.

Here we clarify several important points. First, this study is not about characterizing and parameterizing horizontal mixing/dispersion by mesoscale circulations or eddies, which are associated with horizontal gradients of mesoscale circulations or structures. Rather, it is aimed at horizontal turbulent mixing due to CBL eddies. These large convective eddies are primarily driven by surface heating, not by horizontal mean gradients. For this reason, physics-based horizontal CBL mixing should be linked to the characteristics of these large turbulent eddies, and this study proposes a class of schemes to do so. Second, on the approach taken to parameterize horizontal turbulent mixing, we argue that all conserved variables, subject to mixing by the same CBL eddies, will be mixed horizontally in the same way. In other words, the gradient-diffusion model, which has been shown to work well for passive scalars (INN14), should apply to potential temperature also. The eddy viscosity for momentum may need to be scaled by the turbulent Prandtl number, as the vertical eddy viscosity is. Finally, the schemes proposed in this study are suitable for the same range of grid spacings where PBL schemes are generally applied. Together, they represent turbulent mixing due to boundary layer eddies in the horizontal and vertical directions.

2. Case description and LES setup

The CBL simulation is based on the well-studied Australian Wangara Experiment (Clarke et al. 1971). It describes a time-evolving CBL under baroclinic conditions. The case setup follows Yamada and Mellor (1975). The simulation is from 0900 to 1800 LST for day 33 (16 August 1967) of the experiment. The atmosphere is initialized with an observational sounding at 0900 LST. A time-varying surface flux boundary condition is applied uniformly throughout the simulation domain to drive daytime heating:

$$\begin{aligned} \varphi &= \sin \left[\frac{\pi}{11} (t + 1.5) \right], \\ \overline{w'\theta'_s} &= (0.216 \text{ K m s}^{-1}) \times \varphi, \end{aligned} \quad (1)$$

where $t(h)$ is set to 0 at the beginning of the simulation and $\overline{w'\theta'_s}$ (K m s^{-1}) is the surface sensible heat flux.

Temporally constant geostrophic winds (U_g, V_g) (m s^{-1}) are applied to represent synoptic pressure gradients:

$$\begin{aligned} U_g &= \begin{cases} (0.0029 \text{ s}^{-1}) \times z - 5.5 \text{ m s}^{-1}, & 0 \leq z < 1000 \text{ m} \\ (0.0014 \text{ s}^{-1}) \times z - 4 \text{ m s}^{-1}, & z \geq 1000 \text{ m} \end{cases}, \\ V_g &= 0 \text{ m s}^{-1}. \end{aligned} \quad (2)$$

The ARPS model is used for the simulations. ARPS was developed at the Center for Analysis and Prediction of Storms at the University of Oklahoma. It is a nonhydrostatic mesoscale and convective-scale finite-difference NWP model that is also suitable for LES (e.g., Chow et al. 2005). ARPS uses a generalized height-based terrain-following coordinate on an Arakawa C grid. A mode-splitting time integration scheme is employed (Klemp and Wilhelmson 1978). More details about ARPS are documented in Xue et al. (2000, 2001).

The LES is performed on a doubly periodic domain of $31.2 \text{ km} \times 31.2 \text{ km} \times 2.5 \text{ km}$, with Rayleigh damping applied to the top 500 m of the domain. Such a wide domain is used to provide a large number of samples for horizontal averaging, which minimizes uncertainties of the estimated mean. In particular, a large domain size reduces the scatter of the low-wavenumber end of the horizontal energy spectrum, which allows for computing reliable peak wavelength of the horizontal velocity components, as will be elaborated in section 3. In addition, a large domain size also includes possible submeso- and mesoscale fluctuations that could develop in the potential temperature and specific humidity fields in an evolving CBL (de Roode et al. 2004).

A fine isotropic grid spacing of 25 m is adopted. This 25-m LES is used as the benchmark “truth” for the Wangara CBL. This is justified because the flow on the 25-m LES grid is highly resolved with a negligible contribution from the subgrid scale, except for the first few grid points above the surface. Based on Sullivan and Patton (2011), the CBL is highly resolved (i.e., converges to extremely high-resolution simulations) when the boundary layer depth to grid spacing ratio Z_i/Δ exceeds 60. For the 25-m LES, Z_i/Δ ranges from 53 to 61 from 1400 to 1700 LST, when the CBL is well developed and well resolved. Model results during this time period is selected for the majority of the analyses.

The longitudinal F_{11} and vertical F_{33} energy spectra from the LES at two selected elevations are presented in Fig. 1a to demonstrate the quality of the simulation:

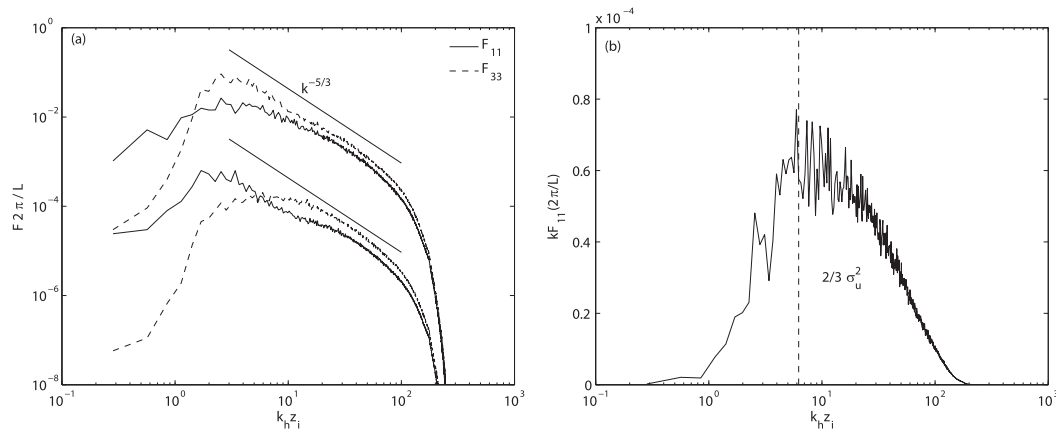


FIG. 1. (a) The longitudinal (F_{11}) and vertical (F_{33}) energy spectra (Tennekes and Lumley 1972, chapter 8) as a function of the normalized horizontal wavenumber $k_h Z_i$. The top two curves are taken at $z/Z_i = 0.5$ and the bottom two from $z/Z_i = 0.1$. For the bottom curves, F_{11} and F_{33} are reduced by two orders of magnitudes for clarity. The two inclined straight lines have slope $k^{-5/3}$. The spectra are normalized by the domain width L . (b) The same F_{11} curve as in (a) at $z/Z_i = 0.5$, but presented on the $\ln(k)$ - kF plot. The vertical dashed line marks the wavenumber up to which 2/3 of the total variance is contained. Results are from 1500 LST.

$$R_{ij}(\mathbf{r}) \equiv \overline{u_i(\mathbf{x}, t)u_j(\mathbf{x} + \mathbf{r}, t)},$$

$$\phi_{ij}(\mathbf{k}) = \frac{1}{(2\pi)^3} \iiint_{-\infty}^{+\infty} \exp(-i\mathbf{k} \cdot \mathbf{r}) R_{ij}(\mathbf{r}) d\mathbf{r}, \quad (3)$$

$$F_{ii}(k_h) = \int_{-\infty}^{+\infty} \phi_{ii}(\mathbf{k}) dk_3.$$

Here, R_{ij} is the correlation tensor, its Fourier transform ϕ_{ij} is the spectrum tensor, F_{ii} is the one dimensional spectrum, \mathbf{r} is the separation length vector in physical space, and \mathbf{k} is the wavenumber vector in Fourier space. The spectra are computed in the horizontal plane only, while the vertical direction is not considered. As shown by Wyngaard (2010, chapter 15.6), the 2D horizontal spectra directly indicate the horizontal spatial scale of eddies contributing to them. The spectra are plotted as a function of the horizontal wavenumber $k_h = \sqrt{k_x^2 + k_y^2}$. The inertial subrange is resolved on the LES grid. Near the surface, the small-wavenumber side of the F_{33} spectrum falls off at a larger wavenumber than the F_{11} spectrum. At higher elevations $z/Z_i = 0.5$, the low-wavenumber end of the F_{33} spectrum rises, indicating the presence of more large scale (relative to the CBL depth) energy. This behavior agrees well with the observed spectra presented in Kaimal and Finnigan (1994, chapter 2). The spectral peak wavelength represents the size of the most energetic convective motions in the CBL. It is best estimated on a wavenumber-weighted spectrum as presented in Fig. 1b. However, the spectral peak can be surrounded by wiggles as shown in Fig. 1b and is difficult to determine objectively. To avoid the noise around the spectral peak, the method of de Roode

et al. (2004) is used, where the peak wavelength is estimated by computing the wavenumber up to which 2/3 of the total variance is contained. The computed peak wavenumber agrees well with the location of the spectral peak as shown in Fig. 1b.

3. Parameterization of horizontal turbulent mixing

The common practice for parameterizing horizontal turbulent fluxes in the PBL in mesoscale models is through the gradient-diffusion model, where

$$\overline{u'\varphi'} = -K_h \frac{\partial \overline{\varphi}}{\partial x} \quad \text{and} \quad \overline{v'\varphi'} = -K_h \frac{\partial \overline{\varphi}}{\partial y}, \quad (4)$$

where φ is a generic variable, $\overline{u'\varphi'}$ and $\overline{v'\varphi'}$ are the subgrid-scale horizontal fluxes, the overbar is an ensemble-average operator, the primes indicate fluctuations from the ensemble mean, and K_h is the horizontal turbulent exchange coefficient for momentum, also known as eddy viscosity. Different mixing coefficients for heat K_h^h and scalars K_h^s are linked by usually predefined turbulent Prandtl (Pr_T) and Schmidt (Sc_T) numbers, and K_h^h and K_h^s are known as eddy diffusivities.

The proposed vertical profile of K_h normalized by the free convective velocity $w_* = [(g/\theta_0)\overline{w'\theta'_s}Z_i]^{1/3}$ and the boundary layer depth Z_i is presented in Fig. 2. The value of Z_i is diagnosed as the elevated level of neutral buoyancy or the equilibrium level for a surface parcel. The derivation of the K_h profile is by diagnosing the characteristic velocity and length scale from LES and will be presented in detail in section 3d. It is introduced here first to enable evaluations of the current

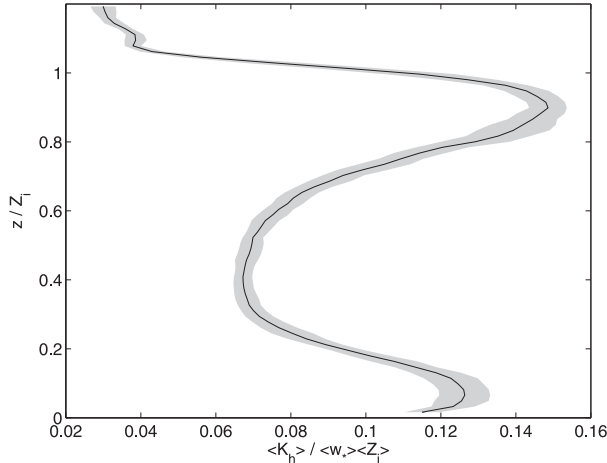


FIG. 2. Vertical profiles of horizontally averaged and time-averaged K_h normalized by the free convective velocity w_* and the boundary layer depth Z_i . Data are from 13 snapshots taken every 15 min from 1400 to 1700 LST. The shading marks plus and minus one standard deviation of the sample mean.

parameterizations for K_h . The choice of the characteristic velocity and length scales for normalization follows INN14. The standard deviation of the sample mean $\sigma_{\langle K_h^* \rangle}$ is computed by

$$\begin{aligned} \overline{\langle K_h^* \rangle}(z^*) &= \frac{1}{N} \sum_{n=1}^N \langle K_h^* \rangle(t_n, z^*), \\ \sigma_{\langle K_h^* \rangle}^2(z^*) &= \frac{1}{N} \sum_{n=1}^N \langle K_h^* \rangle^2(t_n, z^*) - \overline{\langle K_h^* \rangle}^2(z^*). \end{aligned} \quad (5)$$

In Eq. (5), the superscript asterisk indicates normalized variables, where $K_h^* = K_h / (w_* Z_i)$ and $z^* = z / Z_i$. The denominator $N = 13$ is the total number of temporal samples taken at every 15 min from 1400 to 1700 LST. The overbar stands for time averaging, and the angle brackets represent horizontal averaging. The relatively compact $\sigma_{\langle K_h^* \rangle}$ compared to the time-averaged $\overline{\langle K_h^* \rangle}$ suggests that spatial averaging is representative of the ensemble mean. This result benefitted from the wide LES domain that includes a large number of samples, which are the resolved organized convective eddies. More importantly, it indicates that the selected normalization velocity (w_*) and length (Z_i) scales are appropriate for collapsing temporally varying $\langle K_h \rangle$ onto a universal curve $\langle K_h^* \rangle$. In other words, the normalized mean K_h profile shown in Fig. 2 is universal.

The profile of $\langle K_h^* \rangle$ in Fig. 2 is scaled to match that in INN14; it exhibits a C-shaped profile within the CBL. It attains larger values near the surface and toward the top of the boundary layer, while its minimum is found at about $0.4Z_i$. Above the CBL, $\langle K_h^* \rangle$ decreases sharply.

Close to the surface, $\langle K_h^* \rangle$ reaches a local maximum then decreases slightly downward. This is most likely an artifact of the less well-resolved LES flow close to the wall. Similarly, above Z_i , where a strong temperature inversion is found, the LES flow is less well resolved owing to buoyancy damping of turbulence. This is largely responsible for the sudden change of gradient in $\langle K_h^* \rangle$ above $1.1Z_i$. The reason for the degraded quality of $\langle K_h^* \rangle$ in regions where the flow is less resolved is related to its derivation, which will be explained shortly. In INN14, $\langle K_h^* \rangle$ continues to increase toward the surface approaching a value of about 0.12, although its standard deviation is also quite large there. Above the CBL, $\langle K_h^* \rangle$ decreases linearly to 0 at around $1.2Z_i$.

a. Evaluation of current parameterizations

Based on the K_h profile presented in Fig. 2 and in INN14, three current parameterizations of horizontal mixing coefficient are evaluated. Setting K_h to a constant value is a zeroth-order approximation, where vertical variations are ignored. The fundamental issue in such an approach is that it fails to account for the temporal variations of K_h . In Fig. 2, K_h scales with Z_i and w_* , both of which vary with time. Figure 3 presents time series of horizontally averaged Z_i , w_* , and their product. The value of Z_i increases with time as the CBL develops and reaches a maximum at around 1700 LST. The value of w_* increases initially with both the increase of surface heat flux [see Eq. (1)] and the deepening of the CBL. At 1400 LST, w_* plateaus and decreases slowly onward as a result of the decrease in heat flux. Compensated by the continued increase in Z_i , the product $Z_i w_*$ maximizes somewhere between 1500 and 1600 LST. Its value varies by over an order of magnitude from roughly $230 \text{ m}^2 \text{ s}^{-1}$ at 1000 LST to nearly $3000 \text{ m}^2 \text{ s}^{-1}$ at 1500 LST during the course of the day. According to Figs. 2 and 3, setting a constant K_h clearly fails to capture such temporal variations.

A more sophisticated approach for parameterizing K_h is through the 2D Smagorinsky closure (Smagorinsky 1963). For example, in ARPS (Xue et al. 2000) and WRF (Skamarock et al. 2008),

$$K_h = C_s^2 l^2 \sqrt{0.25(D_{11} - D_{22})^2 + D_{12}^2}, \quad (6)$$

where the length scale $l = \sqrt{\Delta x \Delta y}$, C_s is the Smagorinsky coefficient with a WRF default value of 0.25, and $D_{ij} = \partial \bar{U}_i / \partial x_j + \partial \bar{U}_j / \partial x_i$ is the deformation tensor of the resolved flow. In the Community Multiscale Air Quality (CMAQ) model (Byun and Schere 2006), K_h is further constrained for simulations with large (relative to 4 km) grid size to prevent overestimation by

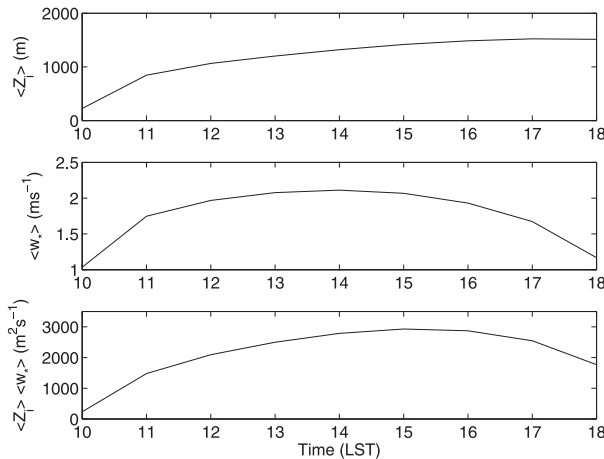


FIG. 3. Time series of horizontally averaged (top) $\langle Z_i \rangle$, (middle) $\langle w_* \rangle$, and (bottom) $\langle Z_i \rangle \langle w_* \rangle$. Statistics are computed at every hour from 1000 to 1800 LST.

$$K_{hN}(\Delta x) = K_{hf}(\Delta x_f) \left(\frac{\Delta x_f}{\Delta x} \right)^2, \quad (7)$$

where $K_{hf} = 2000 \text{ m}^2 \text{ s}^{-1}$ is a prespecified eddy viscosity at a fixed resolution $\Delta x_f = 4 \text{ km}$. Then, $1/K_h$ is obtained as the inverse sum of K_h from Eq. (6) and K_{hN} from Eq. (7).

While the dependence of K_h on the deformation tensor in the original 2D Smagorinsky formulation is intended for horizontal mixing by mesoscale or even larger-scale circulations/eddies (Smagorinsky 1963), its extension to mixing due to PBL turbulent eddies is not well established. For example, in a horizontally homogeneous PBL, an accidental release of an inert contaminant occurs, and an NWP model is used to predict

the downwind dispersion of the contaminant. In the absence of mesoscale horizontal gradients, the horizontal elements of the resolved deformation tensor D , hence K_h , approaches 0 in the mesoscale limit. With $K_h \approx 0$, eddy diffusivity of the contaminant K_h^s also vanishes because of the proportionality relationship $K_h^s = K_h / Sc_T$. Therefore, the mesoscale model predicts no horizontal turbulent mixing of the contaminant, despite the fact that the contaminant field is inhomogeneous, and horizontal turbulent mixing does occur in a horizontally homogeneous flow field, as shown in INN14.

In the thought experiment above, the prediction of horizontal turbulent mixing of a passive scalar in a horizontally homogeneous flow field can be problematic, if eddy diffusivity K_h^s is set proportional to eddy viscosity K_h , and the 2D Smagorinsky scheme is used to predict K_h . To examine the behavior of Eq. (6), the LES field is filtered at successive grid spacings through a sharp Fourier cutoff filter to obtain the deformation tensor evaluated at different scales (spacings). The value of K_h^* is then computed from the filtered LES according to Eq. (6). The K_h^* obtained this way represents the “true” values of the right-hand side of Eq. (6) and, therefore, gives an a priori evaluation of the parameterization.

In Fig. 4a, results from three filter cutoff spacings (i.e., half the filter width) at about 4, 5, and 8 km are presented. Results from wider spacings are not possible because of the LES domain size limit. While the shape of K_h^* profile is in agreement with that presented in Fig. 2, the magnitude decreases at all levels as the filter cutoff spacings coarsen. This suggests that the decrease of the deformation tensor in Eq. (6) overwhelms the increase in the length (grid) scale l , such that their product

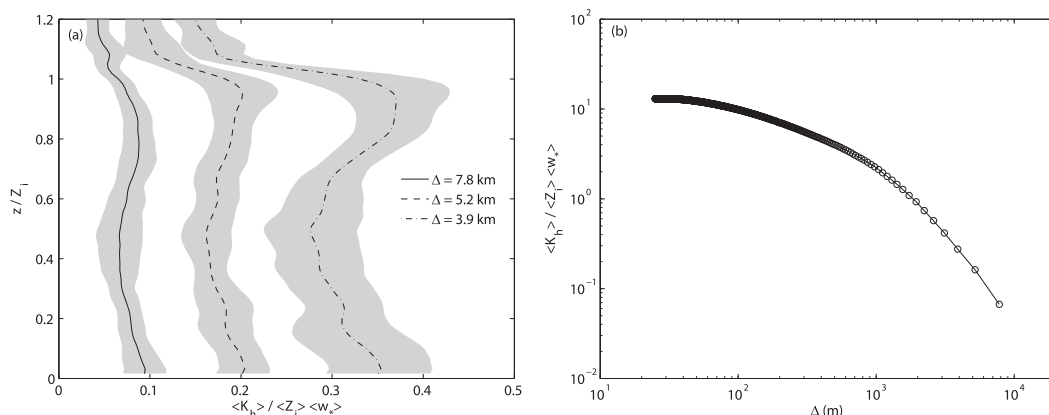


FIG. 4. (a) Vertical profiles of horizontally averaged and normalized $\langle K_h^* \rangle$ at different grid spacings. (b) Variations of $\langle K_h^* \rangle$ as a function of horizontal grid spacing at $z/Z_i = 0.5$. Here, K_h^* is computed according to the 2D Smagorinsky formulation in Eq. (6). Data are from 13 snapshots taken every 15 min from 1400 to 1700 LST. The shading in (a) marks plus and minus one standard deviation of the sample mean.

decreases at larger grid spacings. To further examine the trend in the observed grid dependence, K_h^* is plotted as a function of grid spacing at $z/Z_i = 0.5$ in Fig. 4b (other elevations within the CBL show qualitatively the same behavior). Note that K_h^* decreases monotonically with increasing Δ and does not show signs of convergence at coarse grid spacings. In fact, the rate of decrease in K_h^* (i.e., $dK_h^*/d\Delta$) accelerates toward large spacings. If the curve is extrapolated to around 50-km spacing, an unrealistically small value of $K_h^* \sim 10^{-3}$, or $K_h \sim 1 \text{ m}^2 \text{ s}^{-1}$, is predicted, given typical daytime values of $Z_i = 1000 \text{ m}$ and $w_* = 1 \text{ m s}^{-1}$.

The above results show that in the 2D Smagorinsky formulation, the parameterized K_h^* ceases to matter at large grid spacings. At these spacings, numerical diffusion either implicit with the advection scheme or due to additional computational mixing dominates (Weisman et al. 1997). If computational mixing is adopted, its associated “ K_h ” is effectively set to a constant value (Xue et al. 2000). It then suffers from its indifference to the changes in Z_i and w_* as the CBL develops, which is discussed in the beginning of this subsection. In this case, the parameterized horizontal mixing is of little physical meaning.

Another formulation of K_h is based on the 1.5-order TKE closure (TKE-1.5). This parameterization is directly adapted from the LES closure and has been used in both convective-scale (i.e., $500 \text{ m} < \Delta < 5 \text{ km}$) and mesoscale simulations (Xue et al. 2001; Takemi and Rotunno 2003). Recognizing that the horizontal grid spacing is much coarser than the vertical grid spacing in mesoscale and some convective-scale simulations (i.e., large degree of grid anisotropy), the length scales in the mixing coefficients are set to the horizontal and vertical grid spacings for the respective directions,

$$\begin{aligned} K_h &= 0.1l_h\sqrt{E}, & l_h &= \sqrt{\Delta_x\Delta_y}, \\ K_v &= 0.1l_v\sqrt{E}, & l_z &= \Delta_z, \end{aligned} \quad (8)$$

where E is the subgrid-scale (SGS) TKE and l_h and l_v are the horizontal and vertical length scales (under convective conditions, l_v is linked to the PBL vertical length scale) (Xue et al. 2001). With the filtered LES data, an a priori evaluation of this type of anisotropic TKE-1.5 parameterization for the horizontal mixing coefficient K_h^* is presented in Fig. 5. The shapes of the K_h^* profiles shown in Fig. 5a for three different filter cutoff spacings are nearly identical. Within the CBL, K_h^* is roughly constant with height and decreases sharply toward zero above the CBL top. The profiles of K_h^* for these three spacings are set primarily by the profile of SGS TKE (shown later in Fig. 9). This is because there is almost no

resolved convection on grid scales coarser than 4 km; nearly all TKE is contained in the SGS component. In other words, SGS TKE is saturated as grid spacings approaching 4 km and no longer changes for coarser spacings. As a result, for larger grid spacings, K_h in Eq. (8) scales linearly with l_h , which is set to the horizontal grid spacing. Figure 5b confirms this observation, where K_h^* at the center of the CBL increases linearly with grid spacing at coarse resolutions. Overall, the grid-dependency behavior of K_h^* in the anisotropic TKE-1.5 formulation is the opposite to that of the 2D Smagorinsky formulation. While practically appropriate for convective-scale spacings (Xue et al. 2001; Takemi and Rotunno 2003), the anisotropic TKE-1.5 formulation could overestimate the extent of horizontal turbulent mixing for mesoscale grid spacings.

b. Rationale and limitations of the proposed approach

Before diving into the new schemes, the rationale of the proposed approach and its limitations are discussed. In INN14, a passive scalar field with a constant horizontal gradient is used to trace the effect of horizontal mixing in a homogeneous CBL. The tight error bars in their computed K_h suggest that, at least for passive scalars, the downgradient diffusion approach performs well in parameterizing horizontal scalar fluxes. Since the gradient-diffusion model is appropriate for the representation of horizontal scalar fluxes by CBL mixing, it should also be applicable to potential temperature. This is because both passive scalars and potential temperature are conserved variables in the PBL. When subject to the same turbulent processes, they are expected to be mixed in the same way. Such extension to momentum flux is less certain and likely requires scaling with a turbulent Prandtl number. But strictly speaking, validity of the gradient-diffusion model for representing horizontal mixing of momentum still remains to be tested.

In the following subsections, the gradient-diffusion model is adopted to parameterize horizontal turbulent mixing by CBL eddies. LES-derived horizontal turbulence length and velocity scales are used to formulate turbulent mixing coefficients. The coefficients for scalars, potential temperature, and momentum are not differentiated hereafter.

c. Zeroth-order model for K_h

We propose to define the horizontal turbulent mixing coefficient K_h as a function of characteristic velocity scale v_h and length scale l_h ,

$$K_h(t, \mathbf{x}) = c_h v_h(t, \mathbf{x}) l_h(t, \mathbf{x}), \quad (9)$$

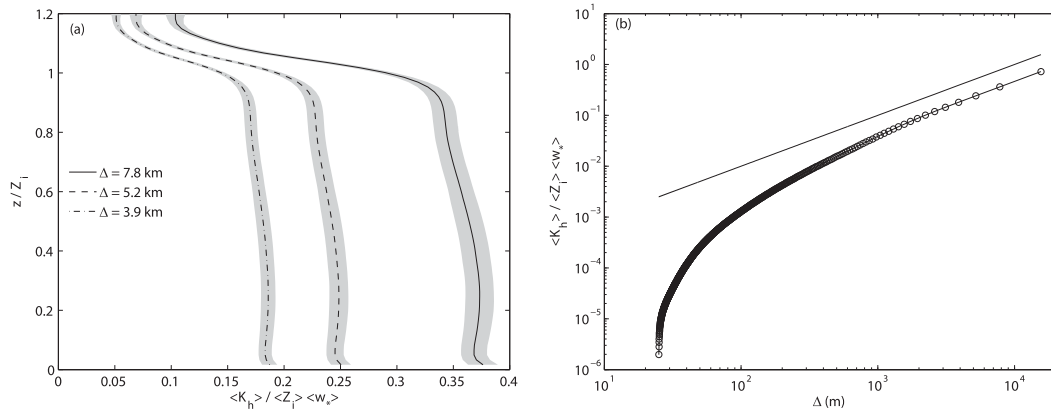


FIG. 5. As in Fig. 4, but for the anisotropic TKE-1.5 parameterization. (b) The solid line marks a linear curve with respect to Δ .

where \mathbf{x} represents (x, y, z) and c_h is a coefficient to be determined. According to INN14, and also as evidenced in Fig. 2, a zeroth-order parameterization for K_h can be formulated by taking w_* and Z_i as the characteristic velocity and length scales. The value of c_h is approximately 0.1, as shown in INN14:

$$K_h(t) = 0.1w_*(t)Z_i(t). \tag{10}$$

Equation (10) is equivalent to setting a constant $K_h^* = 0.1$. This is certainly better than setting K_h to a constant, for it takes into account the temporal variations through w_* and Z_i . Given the vertical variations of K_h^* in Fig. 2, Eq. (10) under- (over-) estimates K_h by around 30% at the top and bottom (center) of the CBL.

In a zeroth-order model, taking Z_i as the characteristic length scale is based on the understanding that organized convective motions, which are responsible for most of the turbulent mixing, span the entire depth of the CBL (Hunt et al. 1988). However, taking w_* as the characteristic velocity scale in Eq. (10) is disputable, because w_* only represents buoyancy-driven turbulence, while shear-induced mixing also plays a part. In other words, when considering characteristic velocity scale for the zeroth-order model, the friction velocity u_* should also be included to form a mixed velocity scale w_s . If we had direct measurements of K_h , we could evaluate the best possible characteristic velocity scale w_s as a combination of (u_*, w_*) by comparing the relative size of the error bars [i.e., the coefficient of variation $\sigma_{(K_h^*)}/\langle K_h^* \rangle$; see Eq. (5)] associated with K_h normalized with different w_s . In the absence of such measurements, the horizontal component of the turbulent kinetic energy $E_h = (1/2)\langle u'u' + v'v' \rangle$ is examined instead of K_h . This is because K_h characterizes mixing due to horizontal turbulent motions, it is only natural to expect that K_h and E_h to share the same characteristic velocity scale.

Wyngaard and Coté (1974) proposed the following relationship for the surface layer,

$$\frac{\sigma_u}{u_*} = \left(12 + 0.5 \frac{Z_i}{|L|} \right)^{1/3}, \tag{11}$$

where $L = -\theta_s u_*^3 / \kappa g \overline{w'\theta'_s}$ is the Obukhov length; κ is the von Kármán constant, usually taken to be 0.41; and g is gravitational acceleration. Using the relation $Z_i/|L| = \kappa w_*^3 / u_*^3$, Eq. (11) is equivalent to

$$E_h^{3/2} = (c_u u_*)^3 + (c_w w_*)^3, \tag{12}$$

where c_u and c_w are 2.3 and 0.59, respectively. Troen and Mahrt (1986) proposed different coefficient values, where $c_u \approx 1.0$ and $c_w \approx 0.65$.

To determine c_u and c_w , $E_h^{3/2}$ is regressed against u_*^3 and w_*^3 at every vertical level in z/Z_i while keeping the intercept zero. In addition, $E_h^{3/2}$ is also regressed against w_*^3 alone to examine the validity of using only w_* as the characteristic velocity scale. Figure 6 presents the regressed coefficients c_w , c_u , and the R^2 value indicating the goodness of fit. The value of c_w decreases from the surface upward and increases back toward the top of the CBL. Its value in the surface layer is about 0.7, which is close to the predicted surface value of 0.65 in Troen and Mahrt (1986). The R^2 values with two variables are close to 1 throughout the depth of the CBL. The profile of c_u shows values around 4.5 with slightly larger values toward the surface and the top of the CBL. It is larger than 1.0 in Troen and Mahrt (1986). This might be related to the Wangara case, which is a weakly sheared, highly convective CBL ($Z_i/|L|$ is roughly 1000 in the afternoon and w_* is about 20 times larger than u_*).

To better test the dependency of the horizontal velocity scale on both u_* and w_* , an additional LES of a

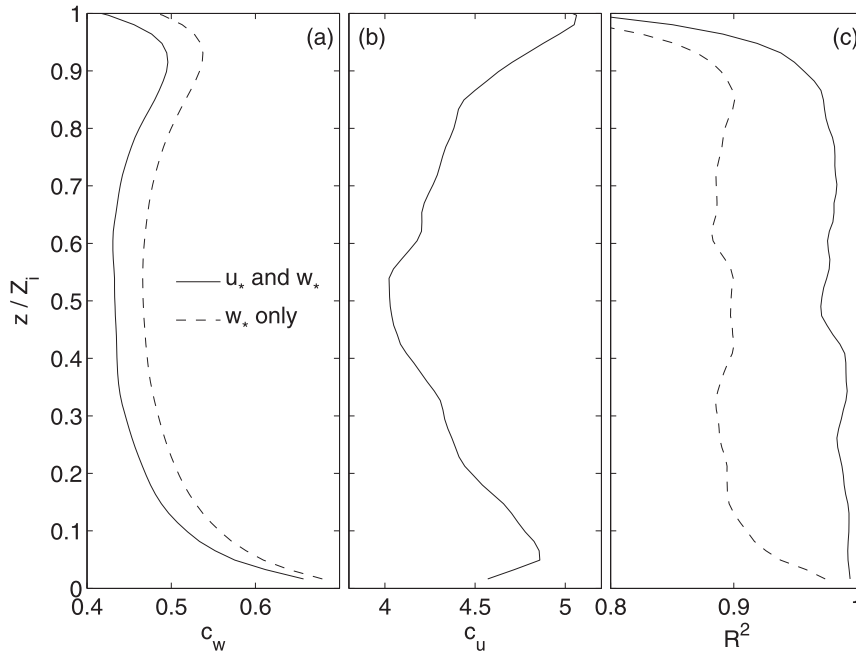


FIG. 6. Vertical profiles of the coefficient (a) c_w and (b) c_u in Eq. (12). (c) Vertical profiles of R^2 for the linear regression. Solid lines represent linear regression including both u_*^3 and w_*^3 . Dashed lines represent regression against w_*^3 only. Data are from 13 snapshots taken every 15 min from 1400 to 1700 LST.

sheared CBL is performed. The simulation setup follows the buoyancy-driven and wind-forced (BF) case of Shin and Hong (2013). The LES adopts 25-m isotropic grid spacing. The model domain is $12 \text{ km} \times 12 \text{ km} \times 2 \text{ km}$ with $483 \times 483 \times 83$ grid points. A constant heat flux of 0.20 K m s^{-1} , along with a barotropic geostrophic wind of 10 m s^{-1} is imposed to drive the sheared CBL. The initial conditions are presented in Shin and Hong (2013) and not repeated here for brevity. The CBL reaches a statistical quasi-steady state after $t_0 = 6\tau$, where $\tau \equiv Z_i/w_*$ is the large-eddy turnover time, approximately 600 s for this case. Results from t_0 to $3t_0$ are used for the analysis. The time and domain-averaged Z_i/L is about 24 for $Z_i = 990 \text{ m}$ and $L = 40 \text{ m}$. In this sheared CBL case, $c_u \approx 0.9$ and $c_w \approx 0.66$. Both are close to values of Troen and Mahrt (1986).

In the Wangara case, using w_* as the only variable in the regression produces a c_w curve that is slightly larger than regressing against both u_* and w_* as shown in Fig. 6. With w_* only, R^2 decreases to 0.9 at about the top of the surface layer, and remains so above. Overall, w_* seems to be a sufficient characteristic velocity scale for the Wangara case, which we adopted for the rest of the paper. The Troen and Mahrt (1986) velocity scale is likely more universal as indicated by the sheared CBL test, although more tests are required to confirm the velocity scale for the zeroth-order model.

d. Length scale-based model for K_h

The next level of parameterization must include the vertical variations in l_h and/or v_h . A physically based choice for l_h is the size of the most energetic horizontal eddies, for they are responsible for the majority of the horizontal mixing. This is inspired by the Sun and Chang (1986) PBL scheme implemented within the ARPS (Xue et al. 1996, 2000), where the vertical characteristic length scale l_v for the vertical mixing coefficient K_v is set to the size of the most energetic vertical motions. The scale l_v is estimated as the peak wavelength of the w spectra λ_w at different elevations, fitted empirically with observations from the Minnesota and Ashchurch experiments (Caughey and Palmer 1979),

$$\lambda_w(z) = 1.8Z_i \left[1 - \exp\left(-4\frac{z}{Z_i}\right) - 0.0003 \exp\left(8\frac{z}{Z_i}\right) \right]. \tag{13}$$

From the Minnesota and Ashchurch experiment data, the peak wavelength of the u and v spectra were simply estimated as $\lambda_u = \lambda_v = 1.5Z_i$,¹ because ‘‘peak

¹ The estimate of $1.5Z_i$ was found in Kaimal (1978), while the quoted comments were made by Caughey and Palmer (1979).

wavelength were difficult to estimate for horizontal velocity components due to considerable scatter at the low frequency end of the spectrum” (Caughey and Palmer 1979, p. 820). In other words, the horizontal flow field likely contained submeso- and/or mesoscale motions that were hard to separate. These large-scale motions were not found in the vertical velocity component, which is consistent with the hypothesis of a spectral gap [see Fig. 2.2 of Stull (1988)].

In our case, the spectral peak wavelengths of u and v can be directly computed from the LES. The wide LES domain reduces the scatter in the small wavenumber end of the spectra and allows reliable estimates of the peak horizontal wavelength λ . The method for computing λ is introduced previously in section 2. The estimated λ s are presented in Fig. 7. The computed λ_w in the Wangara simulation agrees very well with the empirical formulation of Caughey and Palmer (1979) in Eq. (13). The quality of λ_w lends some support to the reliability of the LES and hence the quality of the computed λ_u and λ_v . The peak wavelength for potential temperature spectra λ_θ is also included for completeness. However, λ_θ was not given for the field experiment data, because they failed to show “a consistent pattern” due to the small magnitudes in temperature fluctuations (Kaimal and Finnigan 1994, chapter 2).

In Fig. 7, the profiles of λ_u and λ_v differ slightly only below $0.5z/Z_i$. So herein, $\lambda_{u,v}$ is used to represent both λ_u and λ_v for brevity. The profile of $\lambda_{u,v}$ is also C shaped. It is large toward the surface and the top of the CBL and attains minimum values at around $0.4z/Z_i$. It is known that $\lambda_{u,v}$ is larger than λ_w near the surface, while the difference diminishes into the mixed layer (Kaimal and Finnigan 1994, their Fig. 2.14). An explanation for such a behavior is that, unlike the vertical, the horizontal turbulent motions retain a strong influence from the buoyancy-induced, organized CBL-scale convective structures in the surface layer (Panofsky et al. 1977; Khanna and Brasseur 1998). Therefore, approaching the surface, $\lambda_{u,v}$ retains $O(Z_i)$, while $\lambda_w \sim 5.9z$, which is mainly influenced by shear-induced turbulent eddies that scale with z [Kaimal and Finnigan 1994, Eq. (2.33)]. Toward the top of the CBL, λ_w decreases as a result of the buoyancy-suppressed vertical turbulent motions in the presence of the capping inversion. The horizontal turbulence there is less affected, and $\lambda_{u,v}$ is still of $O(Z_i)$. Presently, we do not have a theory for why $\lambda_{u,v}$ decreases toward the center of the CBL. It is perhaps related to the horizontal advection velocity scale—that is, smaller horizontal velocity creates smaller motion scales.

Given the profile of $\lambda_{u,v}(z/Z_i)$, a parabolic curve fit is found to be satisfactory,

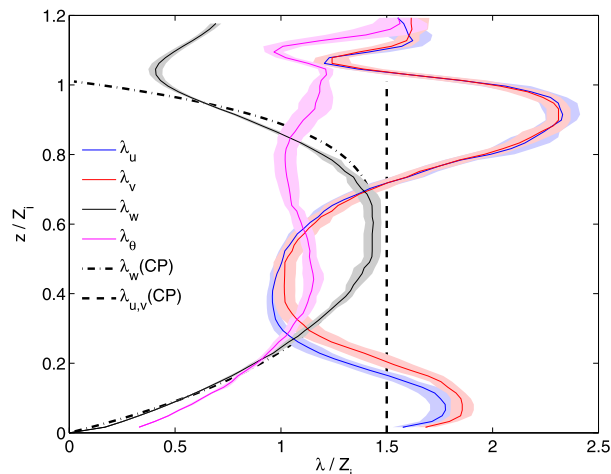


FIG. 7. Vertical profiles of the peak horizontal spectral wavelength. Data are from 13 snapshots taken every 15 min from 1400 to 1700 LST. The shading represents plus and minus one standard deviation of the sample mean.

$$\frac{\lambda_{u,v}}{Z_i} = 7.8 \left(\frac{z}{Z_i} \right)^2 - 6.8 \frac{z}{Z_i} + 2.4, \quad \frac{z}{Z_i} \leq 0.9. \quad (14)$$

As shown in Fig. 8, data between the two dashed lines is used for the curve fit; $\lambda_{u,v}$ close to the surface and the top of the CBL is not used because the flow is less well resolved in these regions. Above $z/Z_i = 0.9$, the fitted $\lambda_{u,v}(z/Z_i)$ is set to decrease linearly to zero at $z/Z_i = 1.2$. The computed $\lambda_{u,v}$ in this depth range is less certain owing to the presence of the capping inversion. A higher-resolution LES is needed to improve the quality of the prediction in these regions. In INN14, the computed K_h also decreases almost linearly from 0.9 to 1.2. This lends some justification for setting the linear decrease in $\lambda_{u,v}$.

The fitted $\lambda_{u,v}$ is used as the characteristic length scale for K_h in Eq. (9). To close the parameterization, a velocity scale must be selected. For a first-order closure, w_* is an appropriate option as discussed for the zeroth-order model in the previous subsection. For high-order closures, the turbulent kinetic energy E is a natural choice. Vertical profiles of all components of $E = (1/2)\langle u'u' + v'v' + w'w' \rangle + \langle E_{\text{sgs}} \rangle$ are presented in Fig. 9; E_{sgs} is the subgrid-scale TKE predicted from a prognostic TKE equation. In Fig. 9, E_{sgs} accounts for only a small fraction of E , again suggesting that the flow field is well resolved. The profiles of $\langle u'u' \rangle$ and $\langle v'v' \rangle$ are similar. They reach maximum values near the surface and decrease to about $0.25w_*^2$ toward the center of the CBL and increase again approaching the top of the CBL. The large values of $\langle u'u' \rangle$ and $\langle v'v' \rangle$ in the surface layer are associated with the local shear

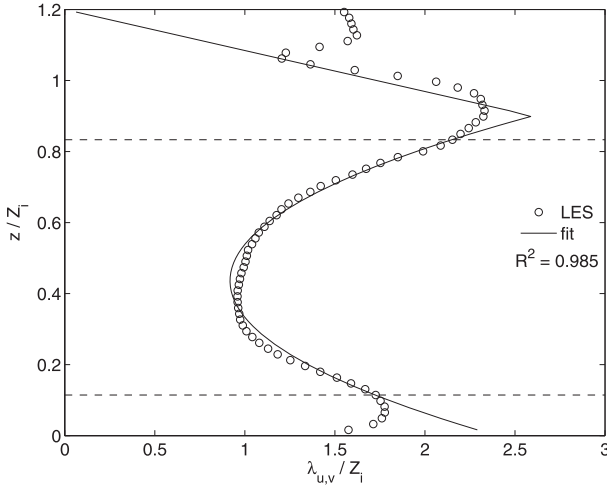


FIG. 8. As in Fig. 6, but for $\lambda_{u,v}/Z_i$ and its parabolic curve fit. Data between the two horizontal dashed lines are used for curve fitting.

production of turbulence, because wind shear is largest in the surface layer, and decreases to zero quickly in the mixed layer. The overall E is about $0.5w_*^2$ near the surface and decreases slightly to $0.4w_*^2$ at the CBL top.

Taking \sqrt{E} and $\lambda_{u,v}$ as the characteristic velocity and length scales, a 1.5-order K_h is formulated:

$$K_h(t, \mathbf{x}) = 0.1\sqrt{E}(t, \mathbf{x})\lambda_{u,v}(t, \mathbf{x}). \quad (15)$$

The coefficient 0.1 is tuned to give the best match to the derived K_h presented in INN14. The result is presented in Fig. 2. Equation (15) is conveniently applied to models that include E as a prognostic variable for its PBL schemes, such as the MYJ (Janjić 1994) and the BouLac (Bougeault and Lacarrere 1989) schemes. It is worth noting that most TKE-based PBL schemes, including the aforementioned ones, compute E from a single column TKE equation in WRF, while in ARPS, the TKE equation is coded in 3D form. The implementation of the horizontal mixing coefficient according to Eq. (15) is certainly more desirable in a 3D rather than 1D TKE equation. For models using first-order PBL schemes, such as the YSU (Hong et al. 2006) and the ACM2 (Pleim 2007) schemes, E in Eq. (15) can be approximated by $0.5w_*^2$ (see Fig. 9) to yield a first-order scheme

$$K_h(t, \mathbf{x}) = 0.07w_*(t)\lambda_{u,v}(t, \mathbf{x}). \quad (16)$$

Equation (16) can be directly applied alongside first-order PBL schemes.

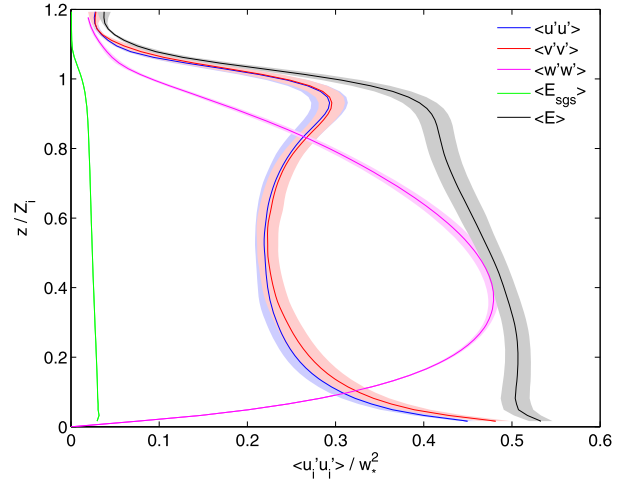


FIG. 9. Vertical profiles of the horizontally averaged and normalized $u_i'u_i'/w_*^2$. Data are from 13 snapshots taken every 15 min from 1400 to 1700 LST. The shading represents plus and minus one standard deviation of the sample mean.

4. A posteriori tests and discussion

a. Experiment setup

To test the proposed schemes for K_h , dispersion of a passive scalar is modeled with ARPS. Simulations of the Wangara CBL are set up on (43, 43, 53) grid points with a uniform horizontal grid spacing of 10 km and a vertical spacing of 50 m. Like the LES run, Rayleigh damping is applied to the top 500 m of the domain. Fourth-order advection schemes are used in both vertical and horizontal directions. Zalesak's multidimensional flux-corrected transport (FCT) scheme is used for scalar advection (Zalesak 1979). This scheme is considered highly accurate for scalar advection because it eliminates both undershoot and overshoot associated with conventional advection schemes (Xue et al. 2000). Random potential temperature perturbations of magnitude ± 0.1 K were added to the first grid level above the wall to initialize the simulations. A list of K_h parameterizations is given in Table 1. To isolate the effects of K_h , computational mixing is switched off.

The Sun and Chang (1986) PBL scheme is used to parameterize vertical turbulent mixing in all model runs. This PBL scheme is based on a prognostic TKE equation. The K_v is parameterized as $0.1\sqrt{E}l_v$, where the vertical mixing length l_v is set to $0.25\lambda_w$ according to Eq. (13). This PBL scheme has been shown to produce good results of the Wangara CBL in Xue et al. (1996, 2001). The proposed formulation of K_h in Eq. (15) can be viewed as an extension of the Sun and Chang (1986) scheme because both use peak spectral wavelengths as characteristic length scales in the parameterization of

TABLE 1. List of models runs with different K_h formulations. In CONS, values for Δx_f and K_{hf} are recommended by [Byun and Schere \(2006\)](#).

Run name	Type	Formulation
CONS	Constant K_h	$K_{hf}(\Delta x_f/\Delta x)^2$, ($\Delta x_f = 4$ km, $K_{hf} = 2000$ m ² s ⁻¹)
SMAG	2D Smagorinsky	$C_s^2 l^2 \sqrt{0.25(D_{11} - D_{22})^2 + D_{12}^2}$
KH0	Zeroth order	$0.1w_* Z_i$
KH1	First order	$0.07w_* \lambda_{u,v}$
KH1.5	1.5 order	$0.1\sqrt{E} \lambda_{u,v}$

the mixing coefficients in their respective directions. For the scalar dispersion study, a passive scalar is introduced as a point source at the east end of the model domain. It is continuously discharged into a surface grid cell at a constant rate from 1200 to 1300 LST. The choice of the source location is entirely arbitrary and does not affect model results in the periodic domain setup.

b. Results and discussion

Vertical profiles of normalized K_h in the experiments at 1500 LST are presented in [Fig. 10a](#). First, notice that the 2D Smagorinsky K_h is a straight line up to around $0.8Z_i$ and has the smallest magnitude than the rest of the profiles. This is very different from the a priori-determined profiles in [Fig. 4](#), where they at least show vertical variations regardless of the magnitude. A closer examination of the flow field reveals that with 10-km grid spacing, there is virtually no resolved flow [i.e., u' is $O(10^{-5})$ m s⁻¹]. The horizontal components of the deformation tensor are close to zero. The predicted K_h is therefore set to the ARPS's built-in minimum threshold K_h^{\min} of $1 \times 10^{-6} \Delta x \Delta y$, in this case 100 m² s⁻¹. Time

series of K_h at 500 m above ground level (AGL) in [Fig. 10b](#) confirms that the 2D Smagorinsky K_h is set to the minimum threshold during the simulation. Experiments are performed at finer resolutions to examine the sensitivity of the 2D Smagorinsky K_h . The model flow field remains quiescent without any resolved flow until 4-km spacing. For all grid spacings coarser than 4 km, the 2D Smagorinsky K_h is set to the minimum threshold regardless of the spacings because of absence of the resolved horizontal deformation. At spacings finer than 4 km, resolved flow develops, and the 2D Smagorinsky K_h is finally active. However, these spacings are considered to be inside the numerical gray zone for CBL convection ([Wyngaard 2004](#)), the validity of the simulated D ; hence, K_h is likely questionable because of the errors of the predicted flow field ([Zhou et al. 2014](#)) and is not discussed here.

The vertical profiles of KH1 and KH1.5 are similar in the lower half of the CBL, but KH1.5 falls off at the top of the CBL owing to the absence of the model predicted subgrid-scale TKE. The profile of KH1 mainly follows that of the fitted $\lambda_{u,v}$ according to [Eq. \(14\)](#). Time series of K_h at 500 m AGL is presented in [Fig. 10b](#) to show its temporal evolution. The temporal trends of all three K_h parameterizations are similar. At 500 m, KH0 is almost twice as large as KH1 and KH1.5. Close to the surface and the top of the CBL, the magnitude of KH1 and KH1.5 are expected to be larger than KH0. The CONS and SMAG cases both give constant K_h ; although the former is by choice, the latter is due to the absence of resolved flow.

Vertical cross section of the tracer concentration S from KH1.5 is presented in [Fig. 11](#). The magnitude of S is related to the source input rate, which is of little relevance in this study. A later time of 1800 LST is chosen here, when the extent of tracer dispersion is maximized.

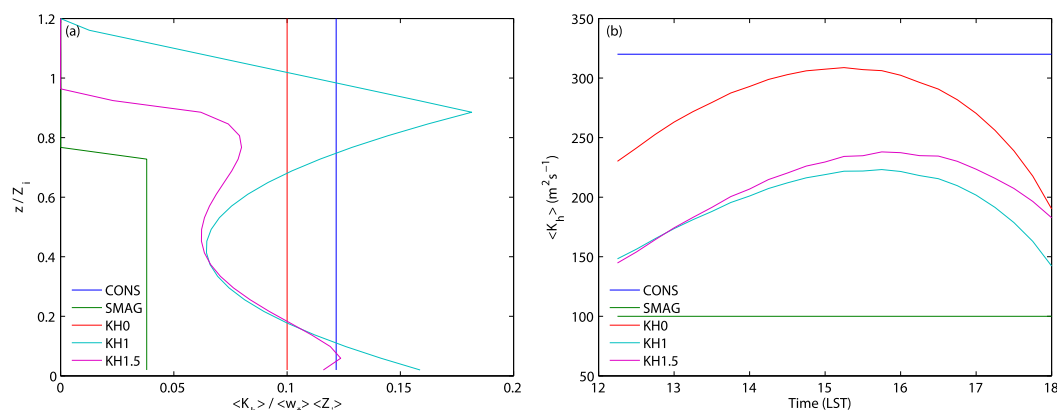


FIG. 10. (a) Vertical profiles of the horizontally averaged and normalized K_h used in various experiments at 1500 LST. (b) Time series of horizontally averaged K_h at 500 m AGL.

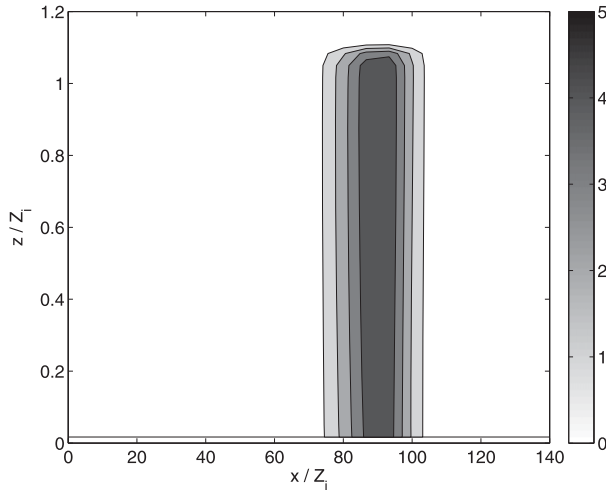


FIG. 11. Vertical cross sections of tracer concentration from the KH1.5 on the x - z plane at 1800 LST. Contour interval is 1 unit.

The distribution of S is nearly uniform in the vertical direction. This is due to efficient vertical mixing by the PBL scheme. In the horizontal direction, the spread of S also does not seem to vary with height, although the K_h profile does vary according to Fig. 10a. The reason why we are not getting a wider spread of S near the surface than the center of the CBL, where K_h is about half of its surface value, is likely attributed to efficient vertical mixing by the PBL scheme. Differences in the horizontal spread of S at different elevations are quickly mixed out in the vertical direction, resulting in a uniform distribution.

To investigate the relative importance of horizontal and vertical mixing, the flux divergence terms in the following prognostic equation for a conserved scalar are presented in Fig. 12:

$$\frac{\partial S}{\partial t} + \frac{\partial u_i S}{\partial x_i} = \underbrace{-\frac{\partial \overline{u's'}}{\partial x} - \frac{\partial \overline{v's'}}{\partial y}}_A - \underbrace{\frac{\partial \overline{w's'}}{\partial z}}_B + S_e. \quad (17)$$

Terms A and B on the right-hand side of Eq. (17) are horizontal and vertical flux divergences that represent the effects of turbulent mixing in the respective directions. The horizontal ($\overline{u's'}$, $\overline{v's'}$) and vertical ($\overline{w's'}$) fluxes are parameterized by gradient-diffusion formulations of Eq. (4). The last term S_e is an external source/sink term. In Fig. 12 the horizontal and vertical scalar flux divergences at 500m AGL at 1800 LST are presented. The left column of Fig. 12 shows results from the proposed 1.5-order scheme (KH1.5), while the right column is from the 2D Smagorinsky scheme (SMAG), which is a popular choice of K_h within the WRF Model for mesoscale applications. The horizontal flux

divergences are negative within and positive outside the tracer plume (see Fig. 11), which indicates a horizontally outward turbulent diffusion. The vertical flux divergences are largely negative, suggesting tracer dilution due mostly to the deepening of the boundary layer.

Comparing magnitudes of the color bars, the horizontal flux divergences (top two panels) are about 5 times smaller than its vertical counterpart (bottom panel) for both horizontal mixing schemes. This suggests that vertical mixing is more important than horizontal mixing for the Wangara case on the 10-km grid. This is in accordance with the vertically uniform scalar concentration presented in Fig. 11. However, at certain places where large horizontal gradient exists (i.e., the edge of the scalar column; see Fig. 11), horizontal flux divergence can exceed vertical flux divergence. For example, at around $(x/Z_i, y/Z_i) = (105, 0)$, the vertical flux divergence is nearly zero in Figs. 12e and 12f, while local maxima are found in the flux divergence along the x direction in Figs. 12a and 12b.

Comparing the left to the right panels reveal differences due to horizontal mixing schemes. The general patterns of flux divergences are qualitatively similar between the KH1.5 and the SMAG schemes. However, the magnitudes of flux divergences of KH1.5 are larger than those of SMAG. This is mainly because K_h for the proposed scheme is larger than that of the 2D Smagorinsky, as shown in Fig. 10. The latter underestimates K_h because of its grid dependency as discussed in section 3a. The differences due to horizontal mixing lead to differences in tracer concentration between KH1.5 and SMAG as presented in Fig. 13. Since K_h of the 2D Smagorinsky scheme is the smallest according to Fig. 10, the resulting S distribution is expected to be narrower with larger peak concentrations. This is reflected in Fig. 13, where at the periphery, S is larger in the KH1.5 run because of its wider spread. The difference field appears skewed as a result of mean wind advection, which is approximately southeasterly for the Wangara CBL. The percentage differences of S among different K_h formulations along the x direction at $y = 0$ are presented in Fig. 14. The constant- K_h case is used as a benchmark, against which all other runs are compared. The 2D Smagorinsky K_h again produces the largest over- and underprediction at the center and the tails of the S distribution, respectively. The percentage relative error between KH1 and KH1.5 cases are similar. Compared to the CONS case, they produce roughly $\pm 10\%$ relative errors. Among the three KH formulations, they differ from each other by around $\pm 5\%$.

Finally, we note that in a horizontally homogeneous background flow such as that of the Wangara test case presented here, the role of horizontal turbulent mixing is

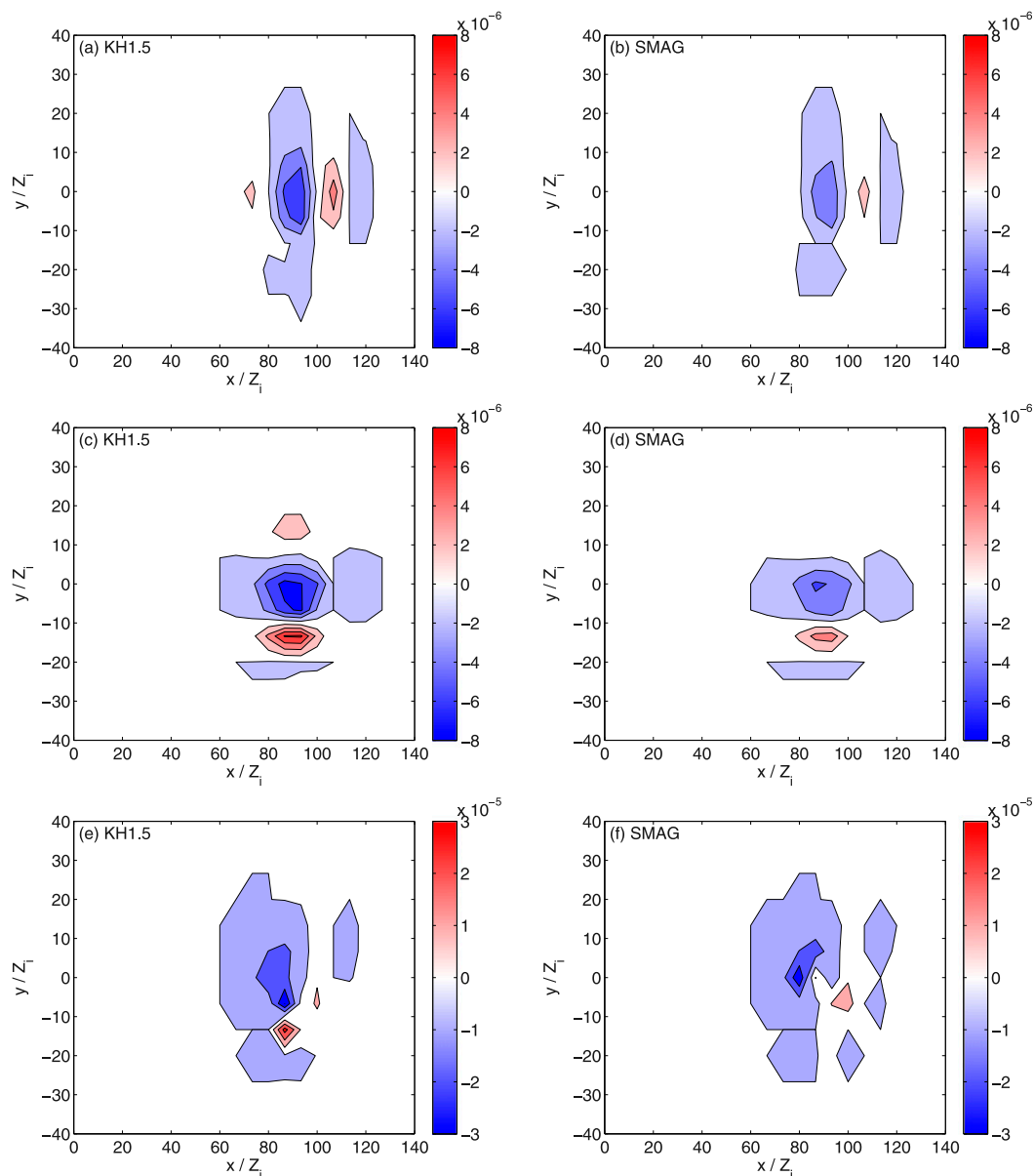


FIG. 12. Contours of turbulent flux divergences in the (a),(b) x , (c),(d) y , and (e),(f) z directions at 500 m AGL at 1800 LST for the scalar diffusion test with 10-km spacing. (left) The KH1.5 scheme and (right) the 2D Smagorinsky scheme. Note that the color bars for the vertical flux divergences in (e) and (f) are different from the other color bars. Contour intervals for the horizontal and vertical directions are 2×10^{-6} and $1 \times 10^{-5} \text{ s}^{-1}$, respectively.

limited compared to its vertical counterpart. Efficient vertical mixing leads to vertically uniform scalar concentrations in Fig. 11, although horizontal mixing can be locally more important than vertical mixing in places of large horizontal scalar gradients as shown in Fig. 12. Horizontal mixing, even though small compared to vertical mixing on a ~ 10 -km grid, still affects the dispersion of scalar concentration as seen in Figs. 13 and 14. The effects of horizontal mixing will be stronger at finer, convection-resolving resolutions. Furthermore,

in a horizontally inhomogeneous background flow, the effects of horizontal mixing would also be more pronounced given the presence of horizontal background gradients.

5. Summary and assessment

This study is devoted to quantifying the effects of horizontal turbulent mixing in the CBL. It is first shown that the traditional parameterizations for horizontal

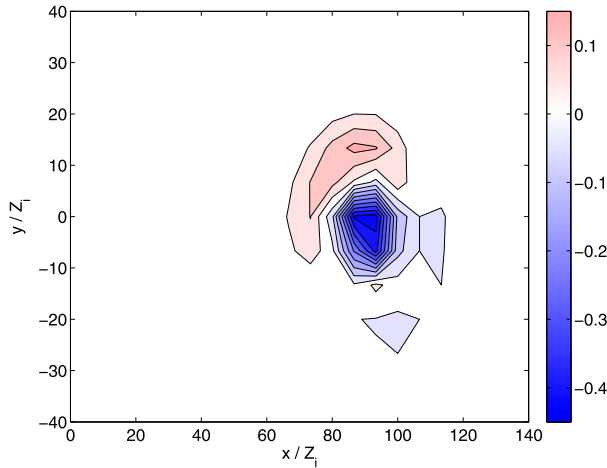


FIG. 13. Horizontal cross section of the difference in the tracer concentration KH1.5 minus SMAG at 500 m AGL at 1800 LST. Contour interval is 0.05 units.

turbulent mixing due to mesoscale circulations/eddies are limited in their representation of mixing due to CBL turbulence. Three commonly used parameterizations for horizontal mixing (i.e., the constant mixing coefficient and the 2D Smagorinsky and the anisotropic TKE-1.5 schemes) are analyzed a priori with filtered LES fields. The constant K_h approach does not account for the state of turbulence in the CBL. Its independence of time is a poor representation of the time-varying K_h associated with the evolution of the CBL. The 2D Smagorinsky scheme is sensitive to the horizontal grid spacings Δ_h . The competing effects of Δ_h and the deformation tensor (i.e., horizontal stretching and shearing) are analyzed. Results show that for a CBL in the absence of mesoscale or synoptic-scale horizontal velocity gradients, horizontal components of the deformation tensor drops quickly. The combined effect is a decrease in K_h with increasing grid spacing. In the a posteriori simulation, the 2D Smagorinsky K_h drops even more quickly than that predicted from the a priori analysis. It remains inactive until the grid spacing is refined to the extent when partially resolved flow starts to appear. The anisotropic TKE-1.5 scheme produces a K_h that scales linearly with horizontal grid spacing Δ_h when Δ_h is large. While it can be tuned through its coefficients to work with convective-scale simulations (Takemi and Rotunno 2003), it will likely overestimate K_h for mesoscale applications.

The limitations of the traditional approach calls for the association of horizontal mixing within the CBL to the characteristics of CBL turbulence. Based on a previous study that reveals good representation of horizontal turbulent scalar fluxes using gradient-diffusion model (INN14), we adopt the gradient-diffusion framework to

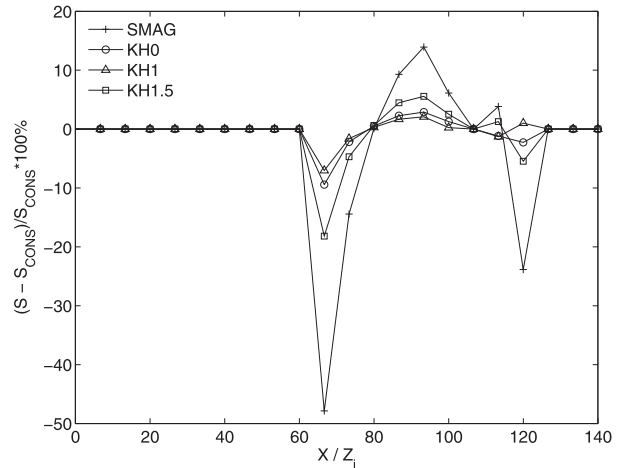


FIG. 14. Percentage relative error $(S - S_{\text{CONS}})/S_{\text{CONS}}$ at 500 m AGL, along the x direction at $y = 0$, at 1800 LST.

parameterize horizontal turbulent mixing of conserved variables including scalar and potential temperature and further extend it to momentum. The turbulent mixing coefficients are then constructed with physically based horizontal turbulence length and velocity scales in a CBL. The simplest K_h uses the free convective velocity w_* and the CBL depth Z_i as characteristic velocity and length scales. It reproduces the temporal evolution of K_h following the development of the CBL but does not include vertical variations of K_h . A more sophisticated first-order formulation uses the dominant length scale of the horizontal turbulent motions, represented by the peak spectral wavelength of the horizontal energy spectra, as the characteristic length scale. It is based on the physical argument that horizontal turbulent mixing is largely achieved by the most energetic eddies. Further improvement of the parameterization is proposed by replacing w_* with the height-varying turbulent kinetic energy \sqrt{E} as the characteristic velocity scale, resulting in a 1.5-order scheme. The coefficients of the parameterizations are determined to best match the derived K_h profile given in INN14.

Among the three, the 1.5-order formulation in Eq. (15) is supposed to be the most accurate since it accounts for the vertical variations of both the characteristic velocity and length scales. However, in the a posteriori tests, vertical mixing is shown to be very efficient in eliminating vertical gradients in the scalar field, such that variations of horizontal scalar dispersion at different elevations are quickly mixed out along the vertical columns, resulting in near-uniform scalar fields. That is to say, strong vertical mixing by the PBL scheme tends to eliminate the need for changes in the vertical profiles of K_h , although this is not expected to hold at convection-resolving resolutions

where horizontal mixing becomes more important. In this sense, the zeroth-order formulation in Eq. (10) might already be sufficient, although small ($\pm 5\%$) differences are still found among the three formulations. In practice, the first-order scheme in Eq. (16) is a more versatile option, since it can be applied alongside any PBL schemes without the need to solve a prognostic TKE equation. Its performance is also close to the 1.5-order scheme.

There are several limitations of the proposed parameterizations. First, the proposed scheme is aimed at horizontal mixing due to CBL eddies. Its performance in the presence of mesoscale horizontal gradients requires further testing. A mixed formulation including one of the proposed schemes and a 2D Smagorinsky scheme might be advantageous to account for combined horizontal turbulent mixing by CBL and mesoscale eddies. Second, the gradient-diffusion model is adopted to parameterize horizontal mixing of scalar potential temperature and momentum. While its application to fluxes of scalars (including conservative potential temperature) is supported by INN14, the extension to momentum is less certain and requires further validation.

In terms of the proposed mixing coefficients, K_h here is derived based on a weakly sheared CBL and without support from field observations. The similarities in the computed K_h profiles to those of INN14 lend some support to our formulation, but the INN14 study is also based on LESs of a CBL with no wind shear. In the absence of field observations of K_h , the next thing worth doing is to perform more LES of the CBL by varying the strength of environmental shear and surface heating and examine the universality of the derived K_h profile. Our additional test of a sheared CBL already shows that the characteristic velocity scales for the zeroth-order and first-order models should adopt a mixed velocity scale of Troen and Mahrt (1986) to include both friction velocity u_* to represent the effects of shear and the free convective velocity w_* to represent the effects of buoyancy. In terms of validation, the idealized scalar diffusion test presented here is far from conclusive. More tests, especially for real cases, should be performed to validate and further improve the proposed formulations.

Strictly, our proposed horizontal mixing parameterizations should be applied beyond the gray-zone grid spacings (i.e., at 4 km and above), like the typical PBL schemes. Below ~ 4 -km grid spacing, the large eddies are partially resolved by the grid so that scale-aware parameterization schemes should be designed and used. For convection-resolving numerical models with horizontal grid spacings of $O(1)$ km, the 3D Smagorinsky

(Lilly 1967) or the 1.5-order TKE (Deardorff 1974) schemes directly adapted from the 3D LES turbulence closures are often used for horizontal mixing (Klemp and Wilhelmson 1978; Xue et al. 2000, 2001). Takemi and Rotunno (2003) examined the effects of subgrid-scale mixing, using the 3D Smagorinsky and the 1.5-order TKE schemes, on idealized simulation of a squall line at 1-km grid spacing. They pointed out that applying these two LES turbulence closures to convection-resolving simulations is inappropriate because 1-km grid spacing is “probably well beyond the inertial subrange” (p. 2098). Nevertheless, they adopted these LES closures for the “lack of a better alternative” (p. 2098). They showed that by tuning the 3D Smagorinsky constants and 1.5-order TKE constants, more satisfactory results could be obtained. Still, in practice, before appropriate scale-aware horizontal PBL turbulence schemes are designed and available, the currently proposed horizontal mixing schemes can be used in combination with a matching vertical PBL scheme, even though within the gray zone they are not ideal. Scale-aware schemes suitable for the gray zone should be developed for both vertical and horizontal mixing at the same time.

Another limitation is that our proposed schemes are for the CBL only. Parameterization for horizontal mixing under neutral or stable conditions is not addressed. Similar LES studies can be carried out following the approach of this work to determine the appropriate length scale and velocity scales for neutral and stable boundary layers, and the corresponding horizontal turbulence parameterizations can be constructed accordingly.

Acknowledgments. We are grateful for the help from Prof. Bob Street for pointing us to the book chapter where Smagorinsky (1993) presented his derivation of K_h for GCMs, which are the contents of his “unpublished manuscript” cited in Smagorinsky (1963). We are grateful to the High Performance Computing Center (HPCC) of Nanjing University for the IBM Blade cluster system where numerical calculations were performed. All authors were supported by the Chinese Ministry of Science and Technology’s 973 Fundamental Research Program (Project 2013CB430103). Bowen Zhou was supported by the Dengfeng Program of Nanjing University, the National Natural Science Foundation of China (Grant 41505047), and a collaborative project on PBL parameterizations with the Beijing Urban Meteorology Institute. Kefeng Zhu was supported by the Foundation of China Meteorological Administration (Grant GYHY201506006) and the National Science Foundation of China (Grant 41405100).

REFERENCES

- Blackadar, A. K., 1962: The vertical distribution of wind and turbulent exchange in a neutral atmosphere. *J. Geophys. Res.*, **67**, 3095–3102, doi:10.1029/JZ067i008p03095.
- Bougeault, P., and P. Lacarrere, 1989: Parameterization of orography-induced turbulence in a mesobeta-scale model. *Mon. Wea. Rev.*, **117**, 1872–1890, doi:10.1175/1520-0493(1989)117<1872:POOITI>2.0.CO;2.
- Bryan, G. H., 2012: Effects of surface exchange coefficients and turbulence length scales on the intensity and structure of numerically simulated hurricanes. *Mon. Wea. Rev.*, **140**, 1125–1143, doi:10.1175/MWR-D-11-00231.1.
- , and R. Rotunno, 2009: The maximum intensity of tropical cyclones in axisymmetric numerical model simulations. *Mon. Wea. Rev.*, **137**, 1770–1789, doi:10.1175/2008MWR2709.1.
- Byun, D., and K. L. Schere, 2006: Review of the governing equations, computational algorithms, and other components of the Models-3 Community Multiscale Air Quality (CMAQ) modeling system. *Appl. Mech. Rev.*, **59**, 51–77, doi:10.1115/1.2128636.
- Caughey, S. J., and S. G. Palmer, 1979: Some aspects of turbulence structure through the depth of the convective boundary layer. *Quart. J. Roy. Meteor. Soc.*, **105**, 811–827, doi:10.1002/qj.49710544606.
- Chow, F. K., R. L. Street, M. Xue, and J. H. Ferziger, 2005: Explicit filtering and reconstruction turbulence modeling for large-eddy simulation of neutral boundary layer flow. *J. Atmos. Sci.*, **62**, 2058–2077, doi:10.1175/JAS3456.1.
- Clarke, R. H., A. J. Dyer, R. R. Brook, D. G. Reid, and A. J. Troup, 1971: The Wangara Experiment: Boundary layer data. CSIRO Division of Meteorological Physics Tech. Paper 19, 340 pp.
- Davidson, G. A., 1990: A modified power law representation of the Pasquill-Gifford dispersion coefficients. *J. Air Waste Manage. Assoc.*, **40**, 1146–1147, doi:10.1080/10473289.1990.10466761.
- Deardorff, J., 1974: Three-dimensional numerical study of turbulence in an entraining mixed layer. *Bound.-Layer Meteor.*, **7**, 199–226, doi:10.1007/BF00227913.
- de Roode, S. R., P. G. Duynkerke, and H. J. J. Jonker, 2004: Large-eddy simulation: How large is large enough? *J. Atmos. Sci.*, **61**, 403–421, doi:10.1175/1520-0469(2004)061<0403:LSHLIL>2.0.CO;2.
- Hong, S.-Y., Y. Noh, and J. Dudhia, 2006: A new vertical diffusion package with an explicit treatment of entrainment processes. *Mon. Wea. Rev.*, **134**, 2318–2341, doi:10.1175/MWR3199.1.
- Hunt, J. C. R., J. C. Kaimal, and J. E. Gaynor, 1988: Eddy structure in the convective boundary layer—New measurements and new concepts. *Quart. J. Roy. Meteor. Soc.*, **114**, 827–858, doi:10.1002/qj.49711448202.
- Ito, J., H. Niino, and M. Nakanishi, 2014: Horizontal turbulent diffusion in a convective mixed layer. *J. Fluid Mech.*, **758**, 553–564, doi:10.1017/jfm.2014.545.
- Janjić, Z. I., 1994: The step-mountain eta coordinate model: Further developments of the convection, viscous sublayer, and turbulence closure schemes. *Mon. Wea. Rev.*, **122**, 927–945, doi:10.1175/1520-0493(1994)122<0927:TSMECM>2.0.CO;2.
- Kaimal, J. C., 1978: Horizontal velocity spectra in an unstable surface layer. *J. Atmos. Sci.*, **35**, 18–24, doi:10.1175/1520-0469(1978)035<0018:HVSIAU>2.0.CO;2.
- , and J. J. Finnigan, 1994: *Atmospheric Boundary Layer Flows: Their Structure and Measurement*. Oxford University Press, 289 pp.
- Khanna, S., and J. G. Brasseur, 1998: Three-dimensional buoyancy- and shear-induced local structure of the atmospheric boundary layer. *J. Atmos. Sci.*, **55**, 710–743, doi:10.1175/1520-0469(1998)055<0710:TDBASI>2.0.CO;2.
- Klemp, J. B., and R. B. Wilhelmson, 1978: The simulation of three-dimensional convective storm dynamics. *J. Atmos. Sci.*, **35**, 1070–1096, doi:10.1175/1520-0469(1978)035<1070:TSOTDC>2.0.CO;2.
- Kormann, R., and F. X. Meixner, 2001: An analytical footprint model for non-neutral stratification. *Bound.-Layer Meteor.*, **99**, 207–224, doi:10.1023/A:1018991015119.
- Lilly, D. K., 1967: The representation of small-scale turbulence in numerical simulation experiments. *Proc. IBM Scientific Symp. on Environmental Science*, White Plains, NY, IBM, 195–210.
- , 1983: Stratified turbulence and the mesoscale variability of the atmosphere. *J. Atmos. Sci.*, **40**, 749–761, doi:10.1175/1520-0469(1983)040<0749:STATMV>2.0.CO;2.
- Nastrom, G. D., and K. S. Gage, 1985: A climatology of atmospheric wavenumber spectra of wind and temperature observed by commercial aircraft. *J. Atmos. Sci.*, **42**, 950–960, doi:10.1175/1520-0469(1985)042<0950:ACOAWS>2.0.CO;2.
- Nazaroff, W. W., and L. Alvarez-Cohen, 2001: *Environmental Engineering Science*. Wiley, 704 pp.
- Panofsky, H. A., H. Tennekes, D. H. Lenschow, and J. C. Wyngaard, 1977: The characteristics of turbulent velocity components in the surface layer under convective conditions. *Bound.-Layer Meteor.*, **11**, 355–361, doi:10.1007/BF02186086.
- Pasquill, F., 1961: The estimation of the dispersion of windborne material. *Meteor. Mag.*, **90**, 33–49.
- Pleim, J. E., 2007: A combined local and nonlocal closure model for the atmospheric boundary layer. Part I: Model description and testing. *J. Appl. Meteor. Climatol.*, **46**, 1383–1395, doi:10.1175/JAM2539.1.
- Pope, S. B., 2000: *Turbulent Flows*. Cambridge University Press, 771 pp.
- Shin, H. H., and S.-Y. Hong, 2013: Analysis of resolved and parameterized vertical transports in convective boundary layers at gray-zone resolutions. *J. Atmos. Sci.*, **70**, 3248–3261, doi:10.1175/JAS-D-12-0290.1.
- Skamarock, W. C., and Coauthors, 2008: A description of the Advanced Research WRF version 3. NCAR Tech. Note NCAR/TN-475+STR, 113 pp., doi:10.5065/D68S4MVH.
- , S.-H. Park, J. B. Klemp, and C. Snyder, 2014: Atmospheric kinetic energy spectra from global high-resolution non-hydrostatic simulations. *J. Atmos. Sci.*, **71**, 4369–4381, doi:10.1175/JAS-D-14-0114.1.
- Smagorinsky, J., 1963: General circulation experiments with the primitive equations. *Mon. Wea. Rev.*, **91**, 99–164, doi:10.1175/1520-0493(1963)091<0099:GCEWTP>2.3.CO;2.
- , 1993: Some historical remarks on the use of nonlinear viscosities. *Large Eddy Simulation of Complex Engineering and Geophysical Flows*, B. Galperin and S. A. Orszag, Eds., Cambridge Press, 3–36.
- Stull, R. B., 1988: *An Introduction to Boundary Layer Meteorology*. Atmospheric and Oceanographic Sciences Library, Vol. 13, Kluwer Academic Publishers, 670 pp., doi:10.1007/978-94-009-3027-8.
- Sullivan, P. P., and E. G. Patton, 2011: The effect of mesh resolution on convective boundary layer statistics and structures generated by large-eddy simulation. *J. Atmos. Sci.*, **68**, 2395–2415, doi:10.1175/JAS-D-10-05010.1.

- Sun, W.-Y., and C.-Z. Chang, 1986: Diffusion model for a convective layer. Part I: Numerical simulation of convective boundary layer. *J. Climate Appl. Meteor.*, **25**, 1445–1453, doi:[10.1175/1520-0450\(1986\)025<1445:DMFACL>2.0.CO;2](https://doi.org/10.1175/1520-0450(1986)025<1445:DMFACL>2.0.CO;2).
- Takemi, T., and R. Rotunno, 2003: The effects of subgrid model mixing and numerical filtering in simulations of mesoscale cloud systems. *Mon. Wea. Rev.*, **131**, 2085–2101, doi:[10.1175/1520-0493\(2003\)131<2085:TEOSMM>2.0.CO;2](https://doi.org/10.1175/1520-0493(2003)131<2085:TEOSMM>2.0.CO;2).
- Tennekes, H., and J. L. Lumley, 1972: *A First Course in Turbulence*. MIT Press, 320 pp.
- Troen, I., and L. Mahrt, 1986: A simple model of the atmospheric boundary layer; sensitivity to surface evaporation. *Bound.-Layer Meteor.*, **37**, 129–148, doi:[10.1007/BF00122760](https://doi.org/10.1007/BF00122760).
- Weisman, M. L., W. C. Skamarock, and J. B. Klemp, 1997: The resolution dependence of explicitly modeled convective systems. *Mon. Wea. Rev.*, **125**, 527–548, doi:[10.1175/1520-0493\(1997\)125<0527:TRDOEM>2.0.CO;2](https://doi.org/10.1175/1520-0493(1997)125<0527:TRDOEM>2.0.CO;2).
- Willis, G. E., and J. W. Deardorff, 1976: A laboratory model of diffusion into the convective planetary boundary layer. *Quart. J. Roy. Meteor. Soc.*, **102**, 427–445, doi:[10.1002/qj.49710243212](https://doi.org/10.1002/qj.49710243212).
- , and —, 1978: A laboratory study of dispersion from an elevated source within a modeled convective planetary boundary layer. *Atmos. Environ.*, **12**, 1305–1311, doi:[10.1016/0004-6981\(78\)90069-0](https://doi.org/10.1016/0004-6981(78)90069-0).
- , and —, 1981: A laboratory study of dispersion from a source in the middle of the convective mixed layer. *Atmos. Environ.*, **15**, 109–117, doi:[10.1016/0004-6981\(81\)90001-9](https://doi.org/10.1016/0004-6981(81)90001-9).
- Wyngaard, J. C., 2004: Toward numerical modeling in the “terra incognita.” *J. Atmos. Sci.*, **61**, 1816–1826, doi:[10.1175/1520-0469\(2004\)061<1816:TNMITT>2.0.CO;2](https://doi.org/10.1175/1520-0469(2004)061<1816:TNMITT>2.0.CO;2).
- , 2010: *Turbulence in the Atmosphere*. Cambridge University Press, 406 pp.
- , and O. R. Coté, 1974: The evolution of a convective planetary boundary layer — A higher-order-closure model study. *Bound.-Layer Meteor.*, **7**, 289–308, doi:[10.1007/BF00240833](https://doi.org/10.1007/BF00240833).
- Xue, M., J. Zong, and K. K. Droegemeier, 1996: Parameterization of PBL turbulence in a multi-scale nonhydrostatic model. Preprints, *11th Conf. on Numerical Weather Prediction*, Norfolk, VA, Amer. Meteor. Soc., 363–365.
- , K. K. Droegemeier, and V. Wong, 2000: The Advanced Regional Prediction System (ARPS) – A multi-scale nonhydrostatic atmospheric simulation and prediction model. Part I: Model dynamics and verification. *Meteor. Atmos. Phys.*, **75**, 161–193, doi:[10.1007/s007030070003](https://doi.org/10.1007/s007030070003).
- , and Coauthors, 2001: The Advanced Regional Prediction System (ARPS) – A multi-scale nonhydrostatic atmospheric simulation and prediction tool. Part II: Model physics and applications. *Meteor. Atmos. Phys.*, **76**, 143–165, doi:[10.1007/s007030170027](https://doi.org/10.1007/s007030170027).
- Yamada, T., and G. Mellor, 1975: A simulation of the Wangara atmospheric boundary layer data. *J. Atmos. Sci.*, **32**, 2309–2329, doi:[10.1175/1520-0469\(1975\)032<2309:ASOTWA>2.0.CO;2](https://doi.org/10.1175/1520-0469(1975)032<2309:ASOTWA>2.0.CO;2).
- Zalesak, S. T., 1979: Fully multidimensional flux-corrected transport algorithms for fluids. *J. Comput. Phys.*, **31**, 335–362, doi:[10.1016/0021-9991\(79\)90051-2](https://doi.org/10.1016/0021-9991(79)90051-2).
- Zhou, B., J. S. Simon, and F. K. Chow, 2014: The convective boundary layer in the terra incognita. *J. Atmos. Sci.*, **71**, 2545–2563, doi:[10.1175/JAS-D-13-0356.1](https://doi.org/10.1175/JAS-D-13-0356.1).